ADVANCED MATERIALS

Supporting Information

for *Adv. Mater.*, DOI 10.1002/adma.202304876

Indoor Photovoltaic Fiber with an Efficiency of 25.53% under 1500 Lux Illumination

*Zhengfeng Zhu, Zhengmeng Lin, Weijie Zhai, Xinyue Kang, Jiatian Song, Chenhao Lu, Hongyu Jiang, Peining Chen, Xuemei Sun, Bingjie Wang, Zhong-Sheng Wang and Huisheng Peng**

ADVANCED MATERIALS

Supporting Information

for *Adv. Mater.*, DOI 10.1002/adma.202304876

Indoor Photovoltaic Fiber with an Efficiency of 25.53% under 1500 Lux Illumination

*Zhengfeng Zhu, Zhengmeng Lin, Weijie Zhai, Xinyue Kang, Jiatian Song, Chenhao Lu, Hongyu Jiang, Peining Chen, Xuemei Sun, Bingjie Wang, Zhong-Sheng Wang and Huisheng Peng**

Supporting Information for

Indoor Photovoltaic Fiber with an Efficiency of 25.53% under 1500 lux Illumination

*Zhengfeng Zhu[1†], Zhengmeng Lin[1†], Weijie Zhai[1†], Xinyue Kang[1], Jiatian Song[1], Chenhao Lu[1], Hongyu Jiang[1], Peining Chen[1], Xuemei Sun[1], Bingjie Wang[1], Zhong-Sheng Wang[2], and Huisheng Peng[1]**

[1]State Key Laboratory of Molecular Engineering of Polymers, Department of Macromolecular Science and Laboratory of Advanced Materials, Fudan University, Shanghai 200438, China.

[2]Department of Chemistry, Fudan University, Shanghai 200438, China.

[†]These authors contributed equally to this work.

Corresponding Email: penghs@fudan.edu.cn

This file includes:

Materials and Methods

All materials, including commercial titanium wire (metal basis: 99.9%, diameter: 140 μm), titanium oxide (anatase, metal basis: 99.8%, size of 30 nm, Aladdin), carboxymethyl cellulose (M.W. 700000, Aladdin), ammonium fluoride (metal basis: 99.99%, Aladdin), ethylene glycol (99.5%, Sinopharm), ethanol (99.7%, Sinopharm), tert-butyl alcohol (99%, Aladdin), acetonitrile (98%, Aladdin), iodine (99.8%, J&K), lithium iodide (anhydrous, 98.5%, J&K), 1,2-dimethyl-3-propylimidazolium iodide (98%, TCI), 4-tert-butylpyridine (96%, Aladdin), acetone (99.5%, Sinopharm), isopropanol (99.7%, Sinopharm), N719 dye (95%, Yingkou OPV Tech New Energy Co., Ltd.) and heat-shrinking tubes (Zhongshan Wolida Electronic Material Co., Ltd.), were commercially available and used without further treatment unless otherwise mentioned.

1. Preparation of fiber photoanodes

A TiO_2 nanotube array on a Ti wire was realized by an anodization process. A Ti wire was cleaned with acetone, isopropanol, and deionized water before being anodized at 60 V and 40 °C in an ethylene glycol solution containing 3.3 g/L NH_4F and 88 g/L H_2O for 0.5–5.5 h. Afterward, the anodized Ti wire was washed with deionized water.

The hybrid TiO_2 layer was made by incorporating TiO_2 nanoparticles into the nanotube array. A TiO_2 nanoparticle slurry was prepared by dispersing TiO_2 nanoparticles (10–30 wt%) and a lower amount of assistant agents into a carboxymethyl cellulose (0.5 wt%) water solution, followed by ball milling at a speed of 500 rpm for 1–4 h. The viscosity of the slurry was effectively augmented by increasing the content of TiO_2 nanoparticles to promote film formation on the fiber. The anodized Ti wire was dip-coated with the slurry at speeds of 0.5–8 m/min and dried in air. The thickness of the TiO_2 nanoparticle film could be simply controlled by the coating speed and cycle.

The above wire was then annealed at 500 °C for 1 h with a heating rate of 8 °C/min starting from room temperature in a furnace. The dye solution of N719 was prepared by dissolving 0.3 mM N719 in tert-butyl alcohol/acetonitrile (1/1, v/v). The fiber photoanode was obtained after the cooled wire was immersed in the dye solution for

24 h.

2. Preparation of fiber counter electrodes

An aligned CNT sheet was prepared by floating catalyst chemical vapor deposition. The feed solution used ethanol as the carbon source mixed with 2.5 wt% ferrocene and 2 wt% thiophene as the composite catalyst. The solution was placed in a furnace at 1200 °C in a hydrogen and argon atmosphere with a flow rate of 0.2 mL/min. The synthesized CNTs were removed from the furnace, densified through water, and dried in air to form an aligned CNT sheet. Then, the CNT sheet was closely attached to a Ti wire at a specific angle to constitute a counter electrode. Moreover, it could be further wrapped with a separator to avoid direct contact with the photoanode.

3. Fabrication of IPVFs

The electrolyte was prepared by dissolving 6 mM I_2, 0.1 M LiI, 0.6 M 1,2-dimethyl-3-propylimidazolium iodide, and 1 M 4-tert-butylpyridine in acetonitrile. To fabricate the IPVF, a fiber photoanode twisted with a fiber counter electrode was encapsulated in a transparent tube (external diameter: 1mm) prepared by extruding melted thermoplastic polymer, then the ends of the tube were sealed by a hot melt adhesive after the injection of electrolyte. Finally, an IPVF with a diameter of 1mm was obtained.

Based on the process parameters, the theoretical production cycle of IPVF and the corresponding output can be calculated. Here, the production cycle of IPVF was ~47.33 h, and the output of each batch of IPVF was ~300 m. According to the formula

$$Tact\ time = \frac{\text{Production cycle } (s)}{\text{Output } (m)},$$

the theoretical tact time was calculated as 568 s/m.

Note that some steps are performed separately for a continuous production of photovoltaic devices at industry. It is fine for the current sensitizing method of IPVFs. In the production of IPVFs, after a batch of fiber electrodes were produced and then put in dye solutions for sensitization, another batch of fiber electrodes could be prepared during this period. The sensitizing time can be fully covered by the production time of fiber electrodes. The unit sensitizing time of fiber electrodes can

be further reduced in the future study.

4. Fabrication of the fiber lithium-ion battery

A fiber positive electrode was prepared by dip-coating a positive slurry (lithium cobalt oxide, super-P, polyvinylidene fluoride, N-methyl-2-pyrrolidone) on an Al wire (diameter of 200 μm). A fiber negative electrode was prepared by dip-coating a negative slurry (graphite, super-P, sodium carboxymethyl cellulose, butadiene styrene rubber, water) on a Cu wire (diameter of 200 μm). The two fiber electrodes were then wrapped with separator strips. The above electrodes were twisted and encapsulated in a tube with injected electrolyte.

5. Characterization

J-V curves of IPVFs were measured with a source meter (Keithley 2420) from 0.7 V to −0.2 V with a scan step of 12.9 mV and a dwell time of 1000 ms under the illumination of a fluorescent lamp (U30). If not otherwise specified, the illuminance of incident light in the measurements was 1500 lux. The intensity of the incident light was tuned by controlling the luminous flux and calibrated by a lux meter (TES-1334A, TES). The lux meter had been calibrated by the National PV Industry Measurement and Testing Center to ensure accuracy and reliability. The emission spectrum of the light was measured by a high-accuracy array spectroradiometer (HAAS-2000, EVERFINE), which had been calibrated strictly by the instrument operation specifications from the manufacturers before measurement. Incident photon-to-current conversion efficiency (IPCE) spectra were measured by an external quantum efficiency (EQE) measurement system containing a power meter (2936-R, Newport) and a monochromator (Cornerstone 260-74125, Newport). During the investigation of the dependence of V_{OC} on the irradiance, neutral density filters were used to tune the irradiance of the light from the solar simulator (Oriel-Sol3A 94023A equipped with a 450 W Xe lamp and an AM1.5 filter, Newport), which was calibrated by a standard silicon solar cell. Absorption spectra of dye solutions and electrolytes and transmittance spectra of the electrolytes were measured by a UV–visible spectrophotometer (Lambda 750, Perkin Elmer). Electrochemical impedance spectra were measured by an electrochemical workstation (CHI 660E, Shanghai Chenhua). Scanning electron microscopy (SEM) images were obtained by a field-emission

scanning electron microscope (Zeiss Sigma, operated at 3 kV). Linear sweep voltammetry measurement of symmetrical cells was performed from −0.70 to 0.70 V with a scan rate of 10 mV/s at room temperature. The involved wearable sensors were common commercial products and operated in strict accordance with the product instructions. The human experiments conformed to the regulation of the Animal and Human Experimentation Committee of Fudan University. A healthy subject from Fudan University had provided written, informed consent before participating in the study.

6. Calculation of the ideality factor (n)

$$n = \frac{q}{k_B T} \frac{\mathrm{d}V_{OC}}{\mathrm{dln}\left(\phi\right)} \quad (1)$$

where n is the ideality factor, q is the elementary charge, k_B is the Boltzmann constant, T is the temperature during the measurement, and ϕ is the irradiance of incident light.

7. Calculation of the power density of indoor light

Briefly, the illuminance of the indoor light on photovoltaic devices, which could be adjusted by varying the distance between the device and the fluorescent lamp, was measured by a commercial lux meter. To calculate the power density of the incident light, we used the following formula:

$$E_V = K_m \int_0^\infty E(\lambda) V(\lambda) d\lambda \quad (2)$$

where E_V is the illuminance (lux, lm/m^2), K_m is a coefficient whose value is 683 lm/W, $E(\lambda)$ is the absolute spectra (W/m^2/nm) of the light, which is the power density as a function of wavelength, $V(\lambda)$ is the standard luminosity function (nm^{-1}) and λ is the wavelength (nm).

We first measured the relative emission spectra ($e(\lambda)$) of the fluorescent lamp with a high-accuracy array spectroradiometer. We assumed that

$$e(\lambda) = mE(\lambda) \quad (3)$$

where m is an unknown coefficient. To calculate the power density of the indoor light with an illuminance of 1500 lux used in this study, we assumed that E_V =1500 lux and took Equation (3) into (2) to perform an integration from 350 to 800 nm. As a result, the value of m and the function $E(\lambda)$ at 1500 lux could be obtained. According to the

formula

$$P = \int_0^\infty E(\lambda)d\lambda \quad (4)$$

where P is the power density (W/m^2) of the incident light, by performing an integration from 350 to 800 nm, we obtained the power density of the incident light at 1500 lux as 423.4 μW/cm^2. The power density of the incident light under other illuminances can be calculated by the same method.

8. Calculation of the PCE of IPVFs

For accurate characterization of the indoor photovoltaic performance of IPVFs, we constructed a special black box fully covered with black light-absorbing layers that could avoid the influence of reflected and scattered light on the measured devices. A fluorescent lamp was set in the black box as a light source, and IPVFs were put under the light. The illumination intensity on IPVFs could be controlled by their relative distances. A lux meter was used to precisely calibrate the illumination on the measured device. In the test, completely lighttight tapes were tightly covered on the needless part of the fiber photovoltaic device as a mask to precisely control the effective illumination area.

The active area of IPVF was represented by the projected area of the photoanode, calculated from its effective length and average diameter. The effective length of the photoanode could be directly measured, while the average diameter was calculated from diameters at different sites along the photoanode.

The PCE of IPVFs was calculated by the following equations:

$$PCE = \frac{J_{SC} \times V_{OC} \times FF}{P_{in}} = \frac{I_{SC} \times V_{OC} \times FF}{A \times P_{in}} \quad (5)$$

$$A = d \times l \quad (6)$$

where I_{SC} is the short-circuit current, P_{in} is the power density of incident light, A is the projected area of the photoanode, d is the average diameter of the photoanode, and l is the effective length of the photoanode.

9. Characterization of the electron transport properties of IPVFs by EIS

A typical equivalent circuit based on the diffusion-recombination model was used to

extract the electron transport parameters of the IPVFs (Figure S7A) [42-43]. The circuit elements related to the photoanode include the electron transport resistance ($R_W = r_W L$) in the TiO_2 layer, charge transfer resistance ($R_K = r_K/L$) at the TiO_2/electrolyte interface, and chemical capacitance ($C\mu = c\mu L$) of TiO_2. Other circuit elements to modify the circuit model include the series resistance (R_S), impedance of the diffusion of I_3^- in the electrolyte (Z_N), charge-transfer resistance (R_{CNT}) and interfacial capacitance (C_{CNT}) at the CNT/electrolyte interface, charge-transfer resistance (R_{Ti}) and interfacial capacitance (C_{Ti}) at the uncovered Ti wire/electrolyte interface, and resistance (R_{TO}) and capacitance (C_{TO}) at the Ti wire/TiO_2 interface. In a typical impedance spectrum, the first high-frequency semicircle is associated with the R_{CNT}, C_{CNT}, R_{Ti}, C_{Ti}, R_{TO} and C_{TO} components. The second semicircle at intermediate frequencies corresponds to the TiO_2 layer, including R_K, R_W and C_μ. The low-frequency arc of the impedance component is derived from the diffusion of I_3^- in the electrolyte (Z_N).

The C_μ resulting from an accumulation of electrons in the TiO_2 region depicts the electron density change at the TiO_2/N719 dye interface, and the total density of free electrons in the TiO_2 conduction band and localized electrons in the trap states, n_T, can then be represented by the equation[44]:

$$C_\mu = \left(\frac{q^2}{k_B T}\right) \times n_T \tag{7}$$

where q is the electron charge and k_B is the Boltzmann constant. A higher n_T may reflect a higher density of electrons in the TiO_2 conduction band that corresponds to an upward shift of the Fermi level of the TiO_2 photoanode causing a higher V_{OC} of the IPVFs.

After extracting the peak frequency (f_{max}) in the middle semicircle related to the TiO_2 layer from the Nyquist plots, the information about the dynamics of photogenerated electrons in the TiO_2 layer, including the effective electron lifetime (τ_n), electron transit time (τ_D), charge collection efficiency (η_{CC}), electron recombination rate (k_{eff}), electron diffusion coefficient (D_n), and effective electron diffusion length (L_n), can be obtained by the following equations[45-47]:

$$\tau_n = (2\pi f_{max})^{-1} \tag{8}$$

$$\tau_D = \left(\frac{R_W}{R_K}\right) \times \tau_n \tag{9}$$

$$\eta_{CC} = \left(1 - \frac{\tau_D}{\tau_n}\right) \times 100\% \quad (10)$$

$$k_{eff} = 2\pi f_{max} \quad (11)$$

$$D_n = \left(\frac{R_K}{R_W}\right) \times L^2 \times k_{eff} \quad (12)$$

$$L_n = (D_n \times \tau_n)^{\frac{1}{2}} \quad (13)$$

where L is thickness of TiO_2 layer.

10. Open-circuit voltage decay (OCVD) measurement of IPVFs

The variation of V_{OC} over time is traced and recorded after the incident light was switched off. The effective electron lifetime (τ_n) can be calculated by the following equation[48]:

$$\tau_n = -\frac{k_B T}{q}\left(\frac{dV_{OC}}{dt}\right)^{-1} \quad (14)$$

where k_B is the Boltzmann constant, T is the temperature, q is the elemental charge, and t is the time.

11. Calculation of the overall energy conversion and storage efficiency of the power system based on IPVFs and fiber lithium-ion batteries

The overall energy conversion and storage efficiency can be calculated according to the following equation[49]:

$$\eta_{overrll} = \frac{E}{P \times S \times t} \times 100\% \quad (15)$$

where E is the discharge energy of the battery (W·h), P is the light intensity (W·m^2), S is the effective area of the photovoltaic cell (m^2), and t is the charging time (h), respectively.

The calculation of discharge energy E is provided by the following equations:

$$E = \int_{V1}^{V2} VCd(v) \quad (16)$$

$$C = I \times t \quad (17)$$

where V_1 and V_2 are the highest and lowest discharge voltages, respectively, while C represents the capacity which is equal to the product of the discharge current (I) and discharge time (t).

According to the dark-discharge curves in Figure 4d, the fiber battery was discharged from 3.8 to 3 V under a discharge current (I) of 0.05 mA with 50 min, then the discharge energy (E) of 0.00011333 W·h was obtained. Taking the area of IPVFs and light intensity into Equation 15, the overall efficiency could be calculated as follows:

$$\eta_{overrll} = \frac{E}{P \times S \times t} \times 100\% = \frac{0.00011333\ W \cdot h}{4.234\ W/m^2 \times 8 \times 0.08\ m \times 0.00018\ m \times 1.25\ h} \times 100\% = 18.59\%$$

12. Statistical analysis

The thickness of TiO_2 nanoparticle layer is defined as half of the difference value between the average dimeters of fiber photoanode before and after dip-coating TiO_2 nanoparticles. PCE value of IPVFs for comparison was presented as the mean ± standard deviation of three measured IPVFs at least. The PCE variation is defined as the standard deviation of PCE divided by its average value.

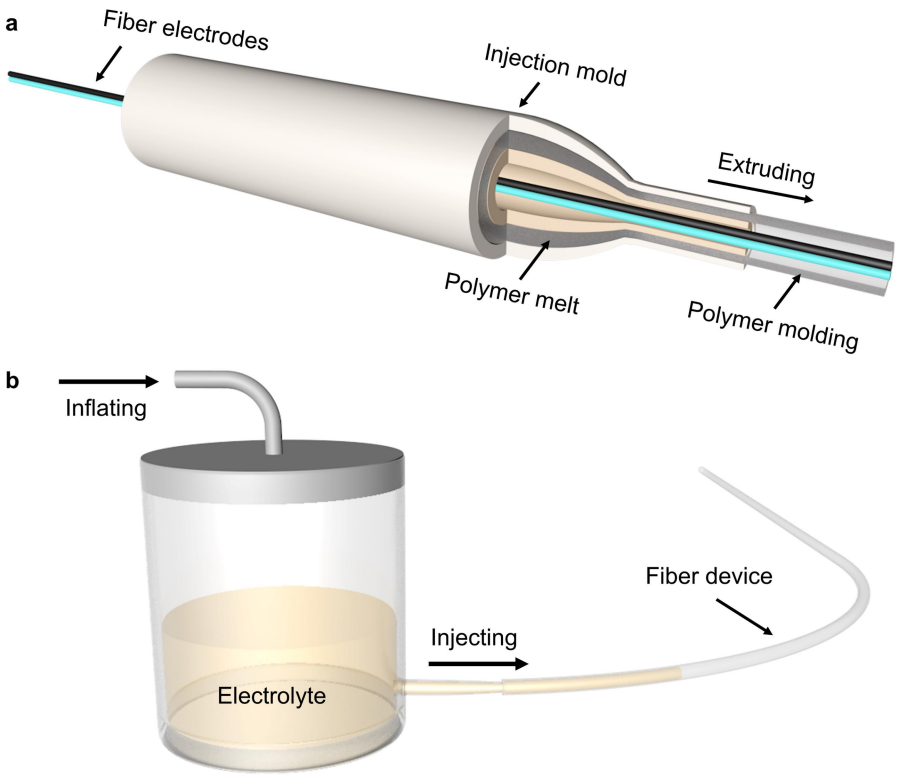

Figure S1. a) Schematic diagram illustrating transparent tube directly made on fiber electrodes. Fiber electrodes can be directly encapsulated in the polymer tube prepared by hot-melt extrusion. b) Schematic diagram of the injecting process. One side of the electrolyte container was tightly connected to the IPVF, and the other side of the container was inflated by a pressure pump, so the electrolyte was efficiently injected into the tube under the gas pressure.

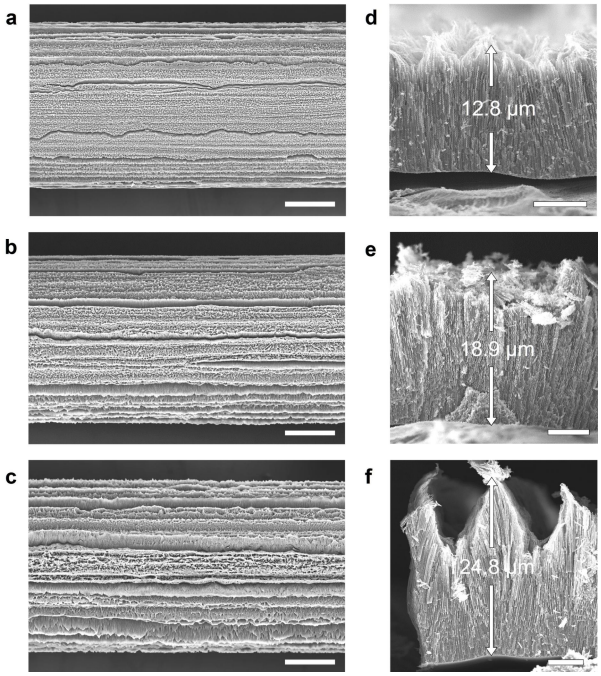

Figure S2. Structures of TiO_2 nanotube arrays anodized on Ti wires. a–c) SEM images showing anodized Ti wires with anodization times of 1 h, 2 h, and 4.5 h, respectively. Scale bars, 50 μm. d–f) Cross-sectional SEM images of TiO_2 nanotube arrays with anodization times of 1 h (d), 2 h (e), and 4.5 h (f). The average thicknesses of the TiO_2 nanotube arrays were accordingly calculated as 12.8, 18.9 and 24.8 μm. Scale bars, 5 μm.

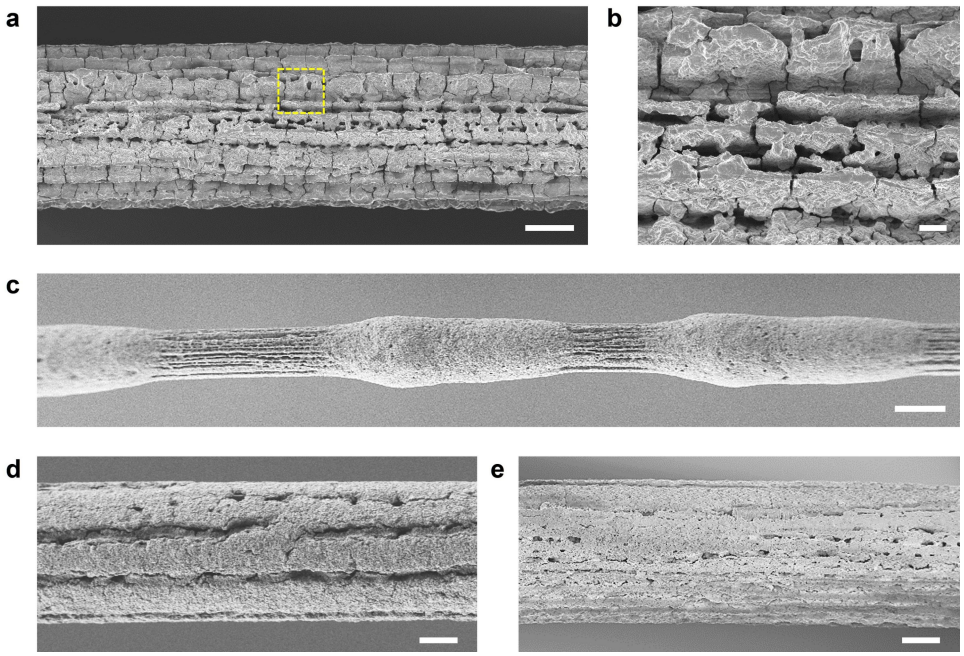

Figure S3. a) SEM images of the TiO_2 nanotube array after dip-coating with a TiO_2 nanoparticle colloidal solution with a viscosity of 0.014 Pa·s. Scale bar, 50 μm. b) Magnified SEM image of the area marked in (a). Scale bar, 10 μm. Monodispersed TiO_2 colloidal solutions are widely used in the planar film formation process, but forming an effective layer on fibers, especially on irregular surfaces, is difficult due to their low viscosity. After dip-coating, TiO_2 nanoparticles mainly gathered around the raised TiO_2 nanotubes instead of forming a film. c–e) SEM images of the TiO_2 nanotube arrays after dip-coating with the as-prepared TiO_2 nanoparticle slurries with TiO_2 contents of 10 wt% (c), 20 wt% (d), and 25 wt% (e), corresponding to slurry viscosities of 0.86, 2.32 and 4.76 Pa·s, respectively. Scale bars, 100 μm in (c) and 50 μm in (d) and (e). The slurry with low viscosity produced obvious agglomeration such as beads on the fiber. The increasing viscosity promoted the slurry covering the TiO_2 nanotube array to form an intact film on the surface.

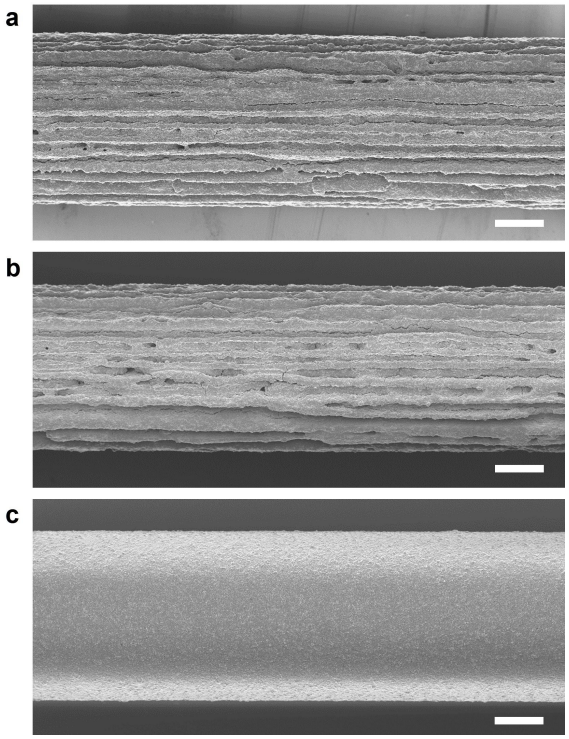

Figure S4. a, b) SEM images of the TiO_2 nanotube arrays partly (a) and fully (b) filled with nanoparticles. c) SEM image of the TiO_2 nanotube array covered with a TiO_2 nanoparticle film. TiO_2 nanoparticles precisely filled in the gaps of the TiO_2 nanotube array and then formed a uniform and smooth TiO_2 layer to construct the hybrid TiO_2 layer with compact interfaces between them. Scale bars, 50 μm.

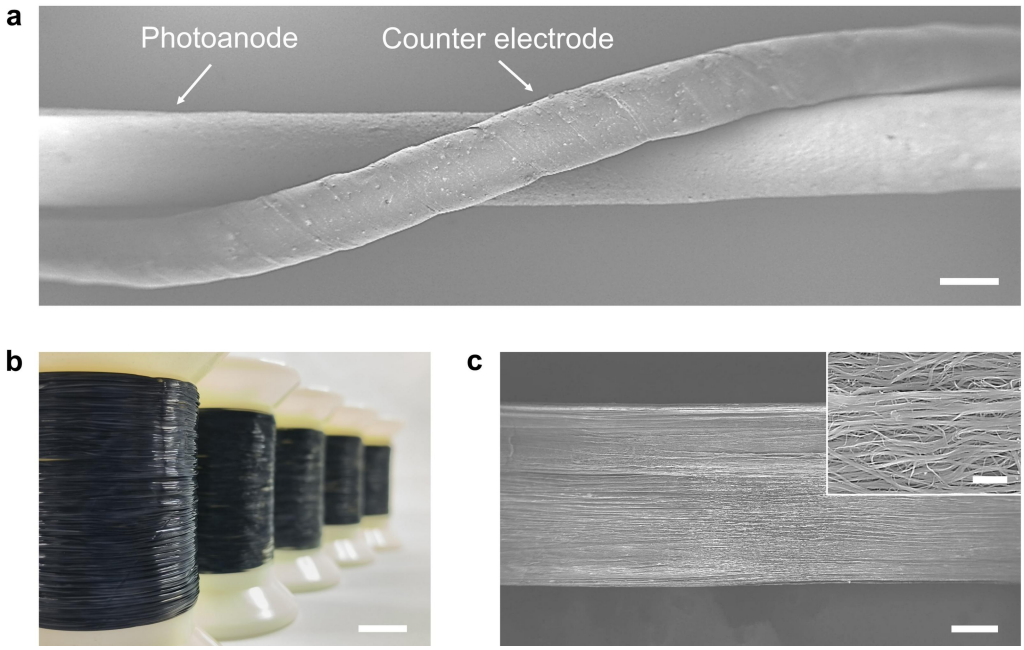

Figure S5. a) SEM image of the structure of the IPVF. Scale bar, 100 μm. b) Photograph of several reels of continuous CNT sheets. Scale bar, 1 cm. c) SEM image of an aligned CNT sheet. Scale bar, 100 μm. Inset of (c), corresponding high-resolution SEM image. Scale bar, 500 nm.

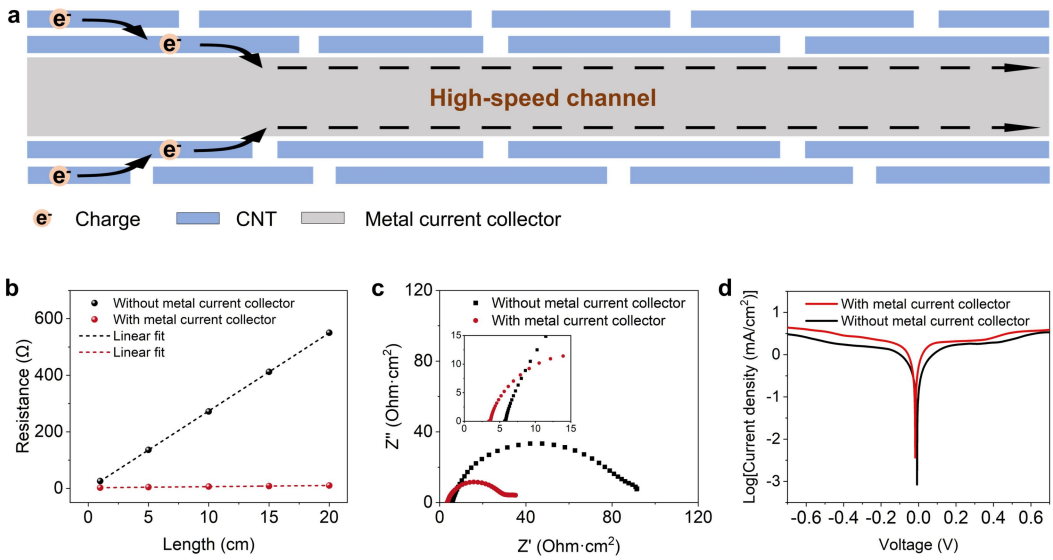

Figure S6. a) Schematic diagram of charge transport in a CNT sheet closely attached to a metal current collector. The charge is rapidly transported along the radial direction through CNTs via a hopping transport mechanism and along the axial direction through the metal channel. b) Electrical resistances of CNT fibers with and without a metal current collector, which were 0.409 and 27.586 Ω/cm, respectively. c) Nyquist plots of symmetrical cells fabricated with two identical electrodes measured at 0 V from 100 kHz to 0.01 Hz in an acetonitrile solution containing 6 mM I_2, 0.1 M LiI, 0.6 M 1,2-dimethyl-3-propylimidazolium iodide, and 1 M 4-tert-butylpyridine. Inset, enlarged view of Nyquist plots at high frequency. The corresponding Nernst diffusion resistances of CNT fibers with and without the metal current collector were 24.19 and 84.46 Ω·cm^2, respectively. d) Tafel polarization plots of symmetrical dummy cells fabricated with two identical electrodes in an acetonitrile solution containing 6 mM I_2, 0.1 M LiI, 0.6 M 1,2-dimethyl-3-propylimidazolium iodide, and 1 M 4-tert-butylpyridine, measured by linear sweep voltammetry. The limiting current densities (J_{lim}) of CNT fibers with and without the metal current collector were 4.36 and 3.03 mA/cm^2, and corresponding diffusion coefficients (D) of I_3^- were 3.767×10^{-4} and 2.621×10^{-4} cm^2/s, respectively.

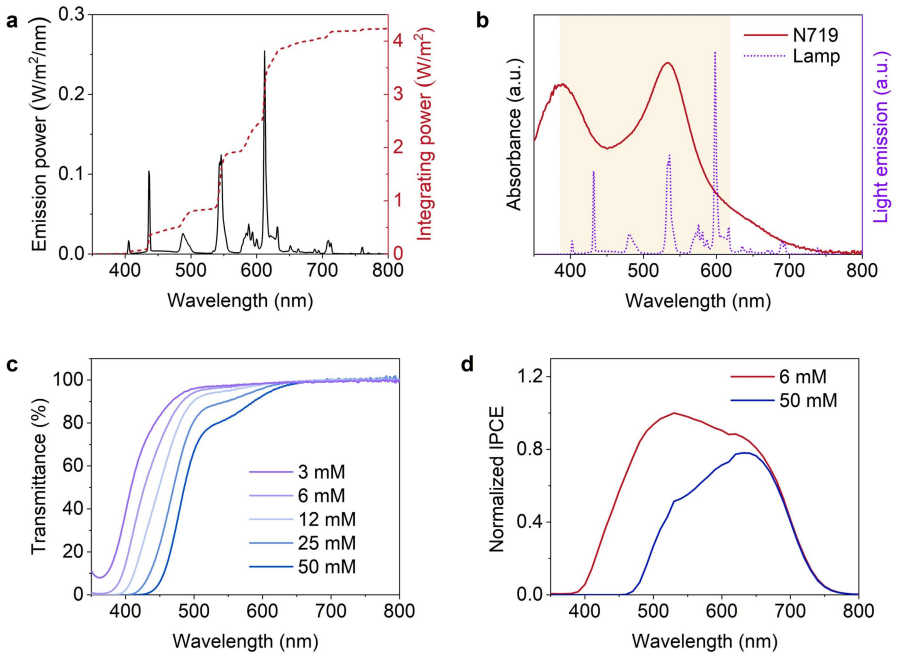

Figure S7. a) Luminescence spectrum of the fluorescent lamp. The integrated intensity under 1500 lux illuminance was 423.4 μW/cm^2. b) UV–visible absorption spectrum of the N719 dye and luminescence spectrum of the fluorescent lamp. c) Transmittance spectra of electrolytes with increasing I_3^- concentration from 3 to 50 mM. d) Normalized IPCE spectra of IPVFs using electrolytes with 6 and 50 mM I_3^- concentrations. The remarkable improvement in photogenerated charge demonstrated efficient light capture at wavelengths of 400–650 nm. I^-/I_3^- redox mediators are widely used in electrolytes but also absorb light in the wavelength range of 400–650 nm, so the incident light across the electrolyte generally suffers additional losses. Because of the much less generated charge under dim indoor light than sunlight, the electrolyte with higher transmittance due to the use of low-concentration I_3^- could be sufficient to support the whole redox system. Therefore, the optimal I_3^- concentration of 6 mM was used in IPVFs for a high photocurrent.

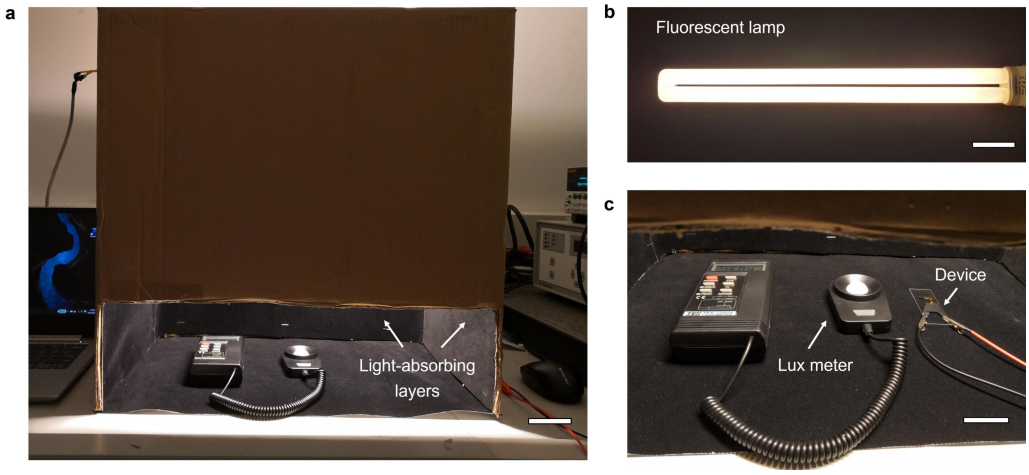

Figure S8. a) Photograph illustrating the test condition for IPVFs. Scale bar, 5 cm. The photovoltaic performances of IPVFs were measured in a specialized black box fully covered with black light-absorbing layers that could avoid the influence of reflected and scattered light on device. b) Photograph of the light source in the black box. Scale bar, 5 cm. A fluorescent lamp was used. c) Photograph illustrating the test procedure. Scale bar, 1 cm. A lux meter was used to precisely calibrate the illumination on the measured device. In the test, completely lighttight tapes were tightly covered on the needless part of the fiber photovoltaic device as a mask to precisely control the effective illumination area.

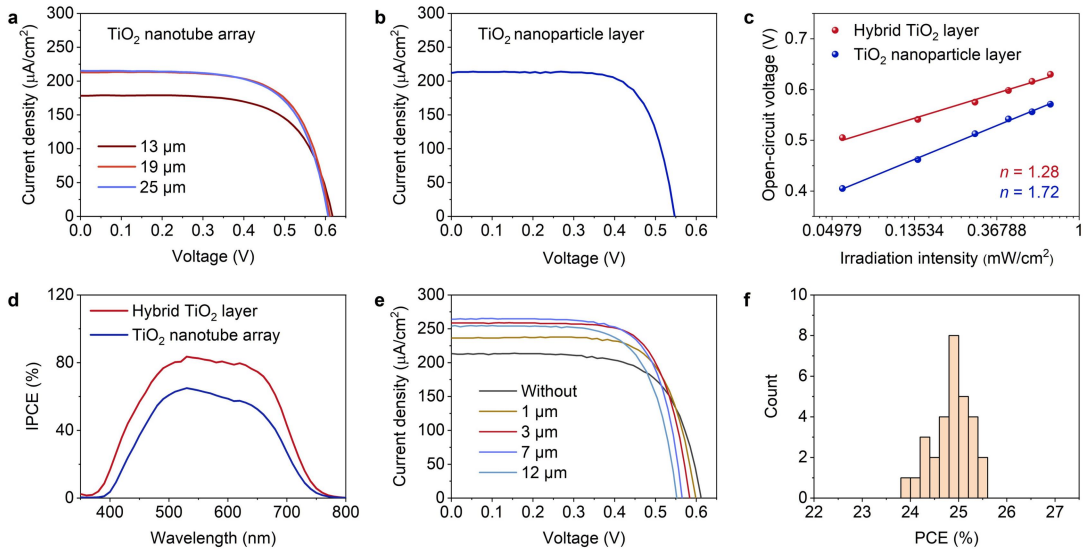

Figure S9. a) *J-V* curves of IPVFs using TiO_2 nanotube arrays with different thicknesses. b) *J-V* curve of IPVFs using the TiO_2 nanoparticle layer, achieving a PCE of 19.72% with a J_{SC} of 214.57 μA/cm^2, a V_{OC} of 0.547 V, and an *FF* of 71.15%. c) V_{OC} of IPVFs using the hybrid TiO_2 layer and TiO_2 nanoparticle layer as photoanodes measured under different irradiation intensities. The corresponding ideality factors were calculated as 1.28 and 1.72 from the red and blue fitted lines, respectively. d) IPCE spectra of IPVFs using the hybrid TiO_2 layer and TiO_2 nanotube array as photoanodes, showing the highest IPCE values of 83.55% and 64.94% at 530 nm, respectively, which demonstrated the marked increase in photogenerated electrons induced by incorporating TiO_2 nanoparticles. Despite the lower light absorption capacity for long-wavelength light of the N719 dye, sufficient dye loading obviously improved light harvesting in the longer wavelength region. e) *J-V* curves of IPVFs using TiO_2 nanotube arrays without and with the incorporation of a TiO_2 nanoparticle layer with increasing thickness. f) PCEs from 30 IPVFs measured under 1500 lux illuminance.

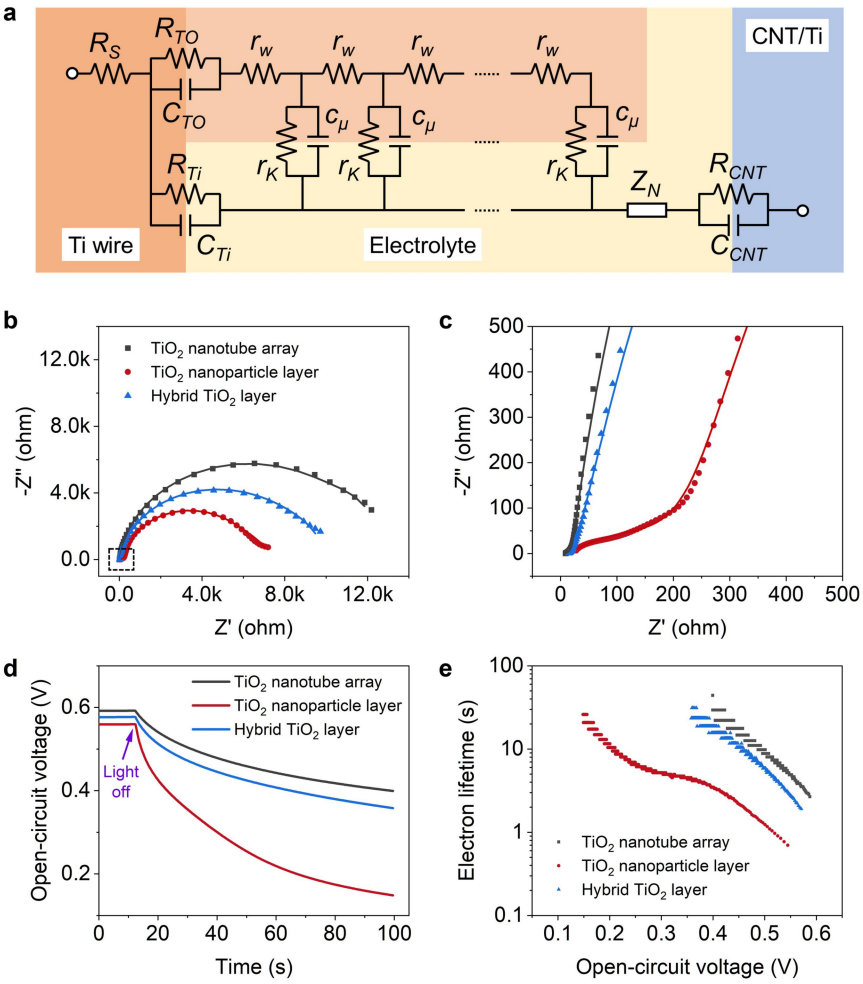

Figure S10. a) Typical equivalent circuit for the simulation of the impedance spectra of IPVFs. b) Nyquist plots and fitted curves of IPVFs with different photoanodes measured under 1500 lux illuminance at the open-circuit voltage. c) Local Nyquist plots marked in (b). The peak frequencies of middle semicircles (f_{max}) were obtained, and a lower frequency reflected a higher electron lifetime. The electron transport resistance ($R_W = r_W L$) in the TiO_2 layer, charge transfer resistance ($R_K = r_K/L$) at the TiO_2/electrolyte interface, series resistance (R_S), and other detailed information about the dynamics of photogenerated electrons in the TiO_2 layer, such as the effective electron lifetime (τ_n), electron transit time (τ_D), charge collection efficiency (η_{CC}), electron diffusion coefficient (D_n), and effective electron diffusion length (L_n), are listed in Table S3. The higher charge transfer resistance reflected the less charge recombination at the TiO_2/electrolyte interface. d) Photovoltage decay plots of IPVFs with different photoanodes after the incident light (1500 lux) was switched off. e) The electron lifetime derived from Equation (14) as a function of V_{OC}.

福建省计量科学研究院
FUJIAN METROLOGY INSTITUTE
（国家光伏产业计量测试中心）
National PV Industry Measurement and Testing Center

ilac-MRA CNAS 中国认可 国际互认 检测 TESTING CNAS L0131

检 测 报 告
Test Report

报告编号：22Q3-00064
Report No.

客户名称 Name of Customer	Fudan University
联络信息 Contact Information	No. 2005, Songhu Road, Yangpu District, Shanghai
物品名称 Name of items	Fiber dye-sensitized solar cell for indoor application
型号/规格 Type /Specification	1 cm
物品编号 Items No	Sample 1
制造厂商 Manufacturer	Fudan University
物品接收日期 Items Receipt Date	2022-03-01
检测日期 Test Date	2022-03-02

福建省计量科学研究院 检测专用章 Stamp 证书/报告专用章 3501020056403

批准人 Approved by 黎健生
核验员 Checked by 何翔
检测员 Test by 陈彩云

发布日期 Date of Report 2022 年 Year 03 月 month 21 日 Day

扫一扫 查真伪

本院/本中心地址：福州市屏东路 9-3 号 Address：9-3 Pingdong Road,Fuzhou,China
电话：0591-87845050 Telephone
传真：0591-87808417 Fax
邮编：350003 Post Code
网址：www.fjjl.net Web Site
咨询电话：0591-87845050 Inquire line
投诉电话：0591-87823025 Complaint Tel

Figure S11a. Scanned copy of the cover page of independent certification report by the National PV Industry Measurement and Testing Center on dye-sensitized photovoltaic fiber for indoor application.

检测结果/说明：
Results of Test and additional explanation.

1 Test Condition:

Total Illuminance: 1500 lux

Temperature: 25.0 ℃

Spectral Distribution: indoor light (U30)

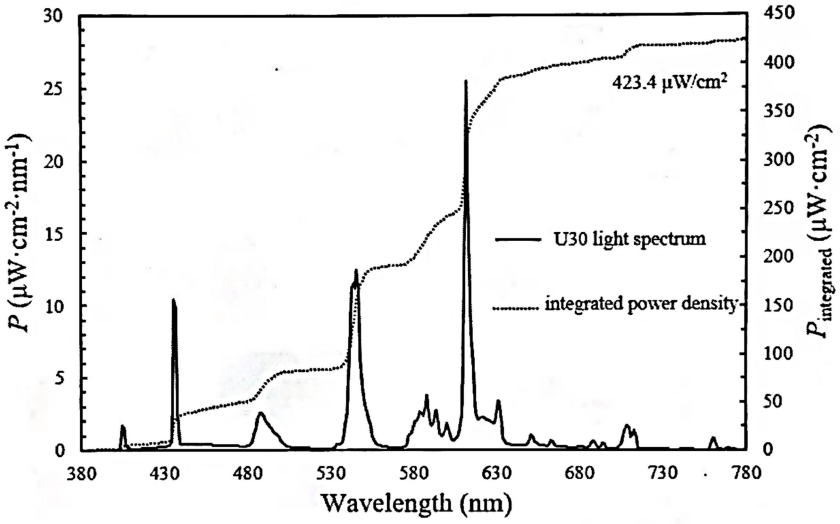

Figure 1. Spectral distribution of indoor light and the corresponding integrated power density

2 Measurement Data and I-V/P-V Curves of Indoor Light under above Test Condition

Reverse Scan

I_{sc} (mA)	V_{oc} (V)	I_{MPP} (mA)	V_{MPP} (V)	P_{MPP} (mW)	FF (%)	η (%)
0.0047	0.5874	0.0041	0.4838	0.0020	72.44	25.53

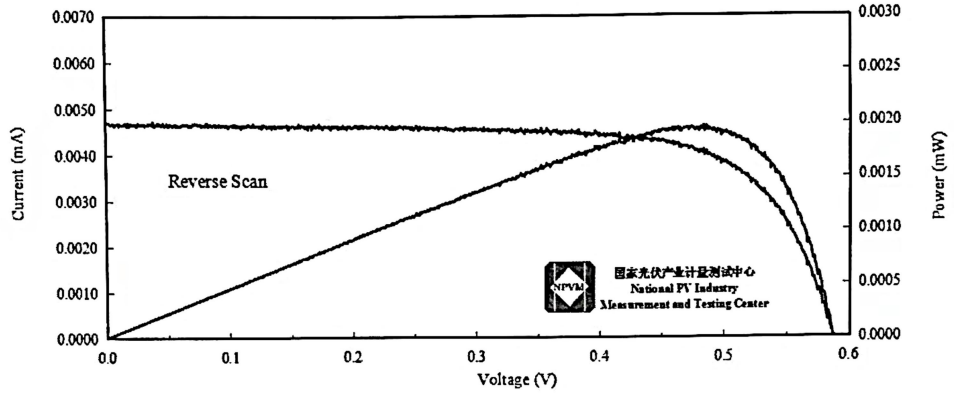

Figure 2. I-V and P-V characteristic curves of the measured sample with indoor light of U30 under STC

Figure S11b. Scanned copy of independent certification report including the information of light source and the measured photovoltaic parameters of certified device.

3 Pictures of the Measured Sample

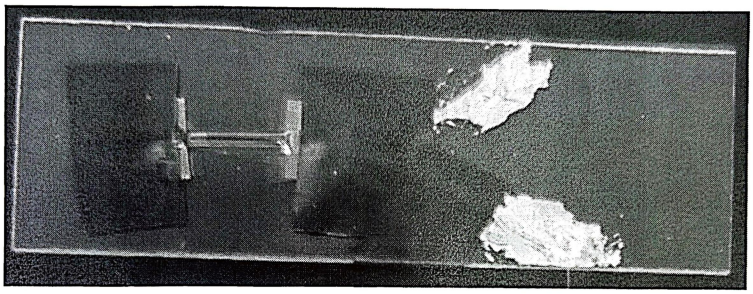

Figure 3. Obverse side of the measured sample

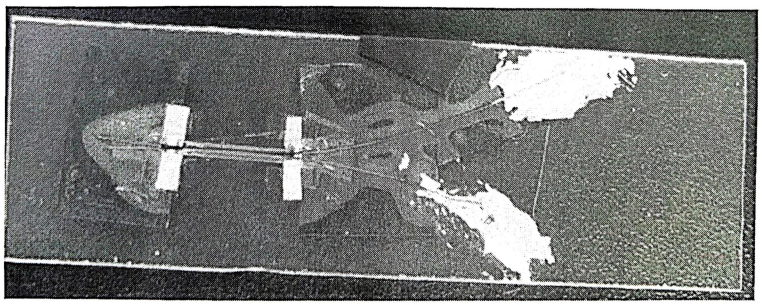

Figure 4. Reverse side of the measured sample

说明：The effective area of the measured sample was 0.0185 cm^2. It was the projected area of the fiber photoanode, which was calculated from its diameter (0.0182 cm) and length (1.0184 cm).

Explanation

Figure S11c. Scanned copy of independent certification report including the photographs of the certified device and the calculation of the effective area. In the measurements, completely lighttight tapes were tightly covered on the needless part of the fiber photovoltaic device as a mask to precisely control the effective illumination area.

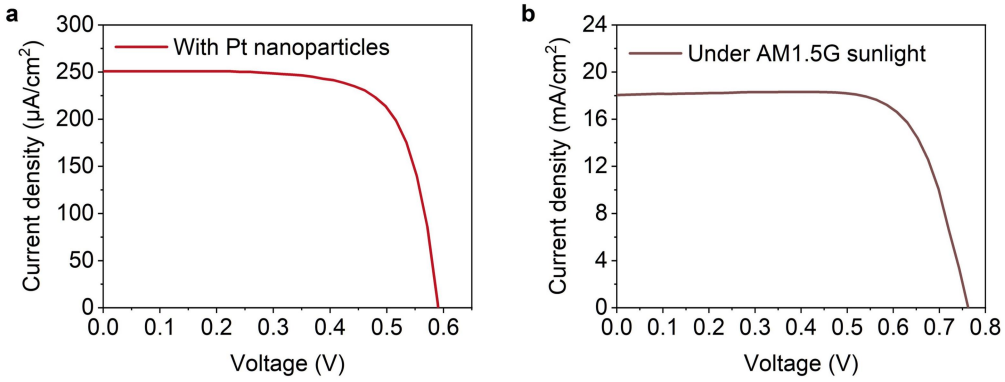

Figure S12. a) *J-V* curve of IPVF with the counter electrode further loaded with Pt nanoparticles, showing a PCE of 25.31%, with J_{SC}, V_{OC}, and *FF* of 252.21 μA/cm^2, 0.588 V, and 72.23%, respectively. b) *J-V* curve of the IPVF using the hybrid TiO_2 layer measured under simulated AM1.5G sunlight, achieving a high PCE of 10.11% with J_{SC} of 18.07 mA/cm^2, V_{OC} of 0.761 V, *FF* of 73.51%.

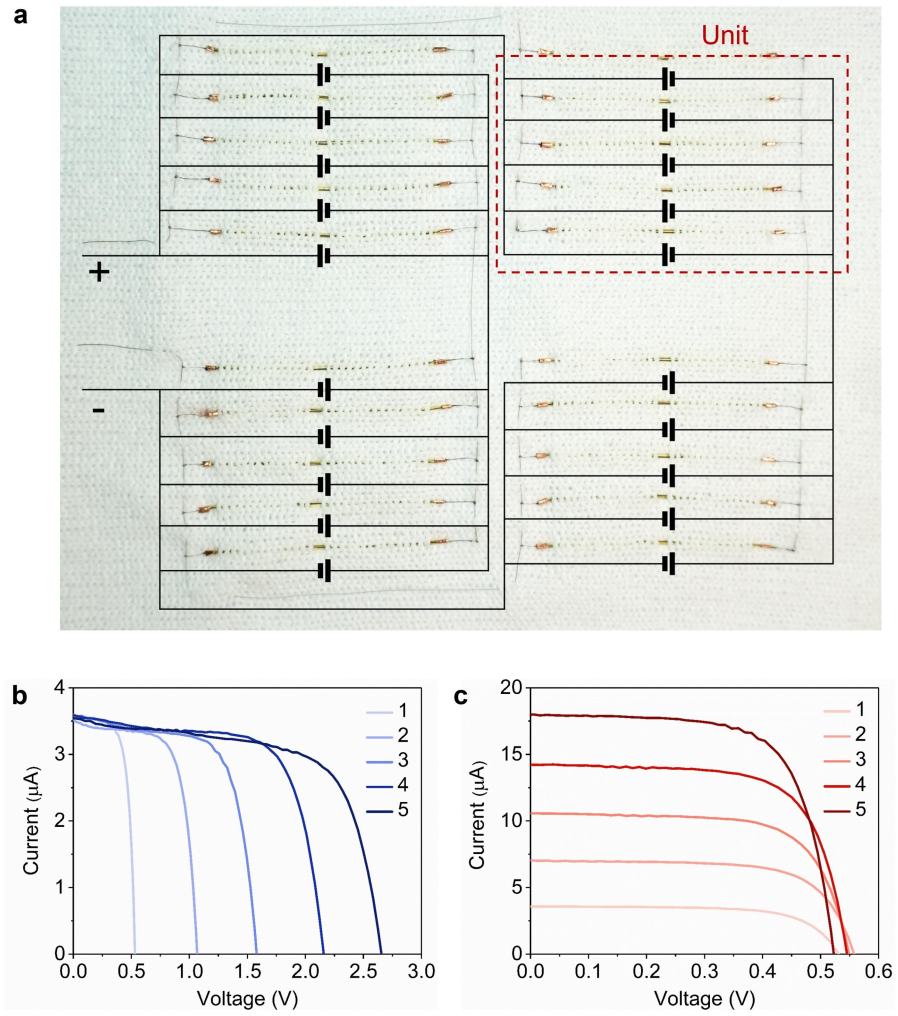

Figure S13. a) Photograph of IPVF modules illustrating their electrical connection in series and in parallel. A unit composed of 5 IPVFs in parallel connection was further connected with other units in series and in parallel for desired output voltages and currents, respectively. b, c) *I-V* curves of IPVFs connected in series (b) and in parallel (c).

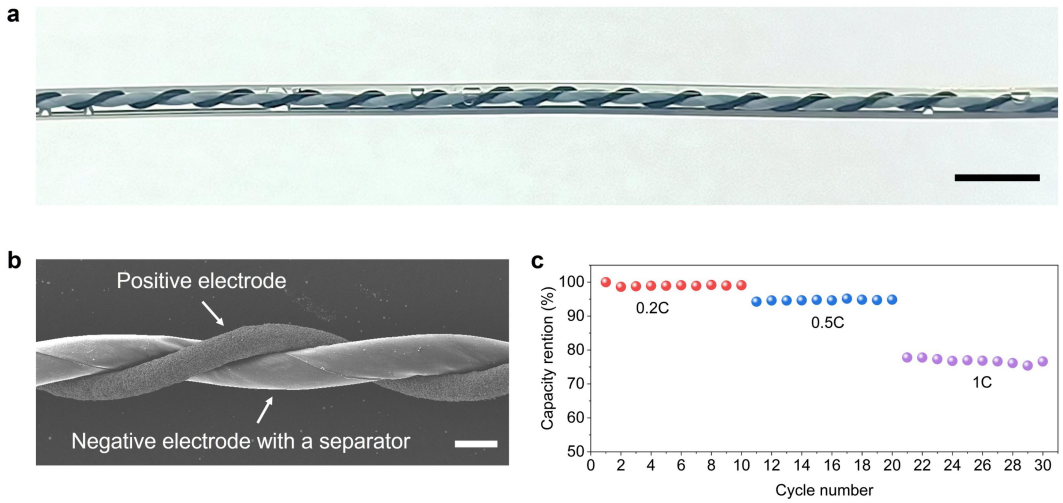

Figure S14. a) Photograph of a fiber lithium-ion battery. Scale bar, 5 mm. b) Corresponding SEM image of inner fiber electrodes. Scale bar, 500 μm. The negative electrode was wrapped with a separator, then twisted with a positive electrode. c) Cycling stability of the fiber lithium-ion battery.

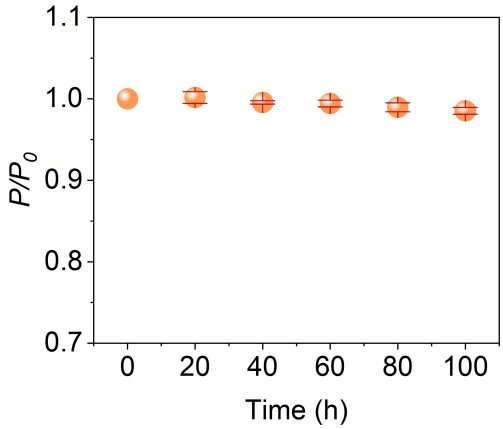

Figure S15. Stability of IPVFs irradiated under a general indoor illuminance of 500 lux continuously. Error bars, standard deviations of the results from three samples. Their PCEs showed a low variation below 5% after the IPVFs were illuminated for 100 h.

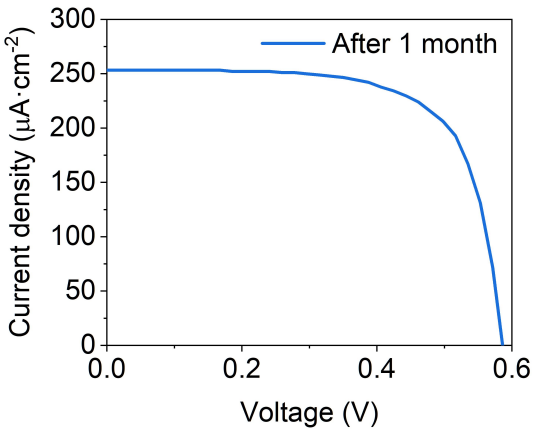

Figure S16. *J-V* curve of the IPVF placed for 1 month. The IPVF showed a high PCE of 24.41% measured under 1500 lux illuminance at 25 ℃, with J_{SC}, V_{OC}, and *FF* of 255.43 μA/cm^2, 0.584 V, and 69.27%, respectively.

Table S1. Photovoltaic parameters of IPVFs in Figure S9a.

Thickness of TiO_2 nanotube array	*Voc*/(V)	*Jsc*/(μA/cm^2)	*FF*/(%)	PCE/(%)
13 μm	0.618	178.30	66.73	17.36
19 μm	0.611	212.79	67.98	20.88
25 μm	0.607	215.86	66.60	20.62

Table S2. Photovoltaic parameters of IPVFs in Figure S9e.

Thickness of TiO_2 nanoparticle layer	*Voc*/(V)	*Jsc*/(μA/cm^2)	*FF*/(%)	PCE/(%)
Without TiO_2 nanoparticle	0.611	212.79	67.98	20.88
1 μm	0.599	235.95	70.93	23.67
3 μm	0.584	260.33	70.54	25.32
7 μm	0.564	264.04	70.91	24.95
12 μm	0.551	254.38	69.02	22.86

Table S3. Electron transport properties of IPVFs with different photoanodes evaluated by EIS.

Photoanode	R_S (Ω)	R_W (Ω)	R_K (Ω)	τ_n (s)	τ_D (ms)	η_{CC} (%)	D_{eff} (cm^2/s, $\times10^{-4}$)	L_n (μm)	n_T (cm^{-3}, $\times10^{17}$)
Bare nanotube array	8.5	45.4	12407	2.83	10.36	99.63	3.48	314.1	1.261
Bare nanoparticle layer	23.6	593	5412	0.74	81.08	89.05	0.40	54.4	0.847
Hybrid layer	13.8	54.2	8451	1.93	12.38	99.36	4.27	287.1	1.259

Table S4. Photovoltaic parameters of IPVFs in Fig. 3b.

Illuminance	*Voc*/(V)	*Jsc*/(μA/cm^2)	*FF*/(%)	PCE/(%)
200 lux	0.496	34.66	69.36	21.20
500 lux	0.535	87.71	69.97	23.21
1000 lux	0.564	172.37	70.58	24.29
1500 lux	0.583	261.80	69.75	25.15

Table S5. Cost analysis of IPVF.

Material	Price USD/g	Weight mg/m	Cost USD/m
CNT	N/A	N/A	0.000788
TiO_2 particle	0.088	7.106	0.00454
Electrolyte	0.560	56.71	0.03176
N719	671.231	0.06	0.04027
Ti wire	0.4149	139.37	0.05782
Encapsulation	0.00194	650	0.00126
other*	N/A	N/A	0.00787
		Total	0.14431

*Include the cost of electricity, water, and anodization process.

Supplementary Reference

[42] F. Fabregat-Santiago, J. Bisquert, E. Palomares, L. Otero, D. Kuang, S. M. Zakeeruddin, M. Grätzel, *J. Phys. Chem. C* **2007**, 111, 6550.

[43] Q. Wang, S. Ito, M. Grätzel, F. Fabregat-Santiago, I. Mora-Sero, J. Bisquert, T. Bessho, H. Imai, *J. Phys. Chem. B* **2006**, 110, 25210.

[44] F. Fabregat-Santiago, J. Bisquert, G. Garcia-Belmonte, G. Boschloo, A. Hagfeldt, *Sol. Energy Mater. Sol. Cells* **2005**, 87, 117.

[45] K. P. Wang, H. Teng, *Phys. Chem. Chem. Phys.* **2009**, 11, 9489.

[46] M. Adachi, M. Sakamoto, J. Jiu, Y. Ogata, S. Isoda, *J. Phys. Chem. B* **2006**, 110, 13872.

[47] Q. Wang, Z. Zhang, S. M. Zakeeruddin, M. Grätzel, *J. Phys. Chem. C* **2008**, 112, 7084.

[48] A. Zaban, M. Greenshtein, J. Bisquert, *ChemPhysChem* **2003**, 4, 859.

[49] Z. Tian, Z. Sun, Y. Shao, L. Gao, R. Huang, Y. Shao, R. B. Kaner, J. Sun, *Energy Environ. Sci.* **2021**, 14, 1602.